Artificial Organs
30(7):539–547, Blackwell Publishing, Inc.

Hemolysis Estimation in a Centrifugal Blood Pump Using a Tensor-based Measure

*‡Dhruv Arora, †*Marek Behr, and ∓‡Matteo Pasquali

**Department of Mechanical Engineering and Materials Science; ∓Department of Chemical and Biomolecular Engineering; ‡Computer and Information Technology Institute (CITI) Rice University, Houston, TX 77005, USA; †Chair for Computational Analysis of Technical Systems (CATS) Center for Computational Engineering Science (CCES) RWTH Aachen University, Aachen, Germany*

Abstract: Hemolysis in the GYRO centrifugal blood pump, under development at the Baylor College of Medicine, Houston, TX, is numerically predicted using the newly proposed tensor-based blood-damage model, as well as a traditional model. Three typical operating conditions for the pump are simulated with a special-purpose finite element-based flow solver, and a novel approach for tracing the pathlines in discretely represented time-varying flow in a complex domain is presented, and 271 pathlines are traced through the pump. Hemolysis is computed along the pathlines, and the accumulated hemolysis at the outflow is converted into standard clinical units. The cumulative hemolysis at the outlet of the pump is weighted with the flow rate associated with the pathlines, and a temporal average is obtained by releasing the tracer particles at different time intervals. Numerical predictions are compared to experimental hemolysis studies performed according to the American Society for Testing and Materials standards at the Baylor College of Medicine. The tensor-based blood-damage model is found to match very well with the experimental results, whereas the traditional model overpredicts the hemolysis. The success of the tensor-based blood-damage model is attributed to its construction, which accounts for blood-specific physical properties and phenomena. Hemolysis values at the typical operating conditions of the pump are found to be within the clinically accepted range.
Key Words: Ventricular assist device—Computational fluid dynamics—Red blood cell—Hemolysis—Normalized index of hemolysis—Wall distance.

1 INTRODUCTION

Application of computational fluid dynamics (CFD) to ventricular assist device (VAD) design has shortened the hydraulic design cycle time, and further reduction is expected through development of reliable and accurate virtual hemolysis prediction techniques (1).

Traditionally, VADs were designed based on insights from Newtonian fluid mechanics, and adapted for blood through in vivo animal experiments; this process was time-consuming and expensive. With the advances in computational resources and robust numerical schemes, CFD has emerged as a reliable design tool for hydraulic design of blood pumps, which accurately predicts performance and flow characteristics (2). Hematologic design of the pump is equally important; blood damage (hemolysis) and blood coagulation (thrombosis) are both important aspects of the hematologic design. A clear understanding of these processes in complex flows of blood-handling devices is yet to be formed, and consequently, a reliable blood-damage model for numerical predictions is not yet available.

Based on the review of mechanical shear hemolysis experiments (3–6) and numerical studies (7–11), the following characteristics are considered desirable in an ideal blood-damage model:

1 The physical properties of blood must be accounted for resulting in a hemolysis model that is blood sample-specific. For example, the mean cell volume (MCV) for RBCs vary from species to species ($MCV_{human\ blood} > MCV_{bovine\ blood}$) and the hemolysis model should account for this difference. Moreover, the phenomena associated with blood, for example, the tank-treading motion (12), should also be taken into account.

Received October 2005; revised February 2006.
Address correspondence and reprint requests to Dr. Dhruv Arora, Department of Mechanical Engineering & Materials Science—MS 321, Rice University, PO Box 1892, Houston, TX 77251-1892, U.S.A. E-mail: dhruv@rice.edu

2 Blood flow conditions (e.g., the hemo-incompatibility of blood-contacting surfaces, blood-air contact, thermal hemolysis, etc.) can affect hemolysis measurements and the model should be sensitive to these effects.

3 The numerical hemolysis predictions must be consistent with both steady and unsteady simple shear hemolysis data. This implies that the model should capture the red blood cell (RBC) behavior in the flow, and account for the viscoelastic nature of blood. Presently, there is a shortage of unsteady simple shear flow hemolysis data in the literature.

4 The model must be three-dimensional (3D) in construction in order to account for the complex flow features in common blood-handling devices. In other words, the model should be related to the rate-of-strain and vorticity tensors.

5 From the implementation perspective, the model should be simple to integrate into the CFD analysis. Moreover, the numerical hemolysis predictions should be easily translated into standard clinical metric of hemolysis—the normalized index of hemolysis (NIH) (13) for direct experimental validation.

In general, hemolysis in a steady simple shear flow experiment can be related to the shear rate and exposure time through a power-law form. The most commonly used correlation for steady simple shear experiments is the one proposed by Giersiepen et al. (6), which is valid for time scales relevant to flows in blood pumps:

$$\frac{\Delta Hb}{Hb} = 3.62 \times 10^{-7} \sigma^{2.416} \Delta t^{0.785}, \qquad (1)$$

where $\frac{\Delta Hb}{Hb}$ is the ratio of plasma-free hemoglobin (pfHb) to the total hemoglobin in the sample, σ is the shear stress (Pa), and Δt is the exposure time (s).

It is important to note that σ in correlation (1) refers to the steady shear stress. In the past, several studies applied (1) to compute hemolysis in complex 3D transient flows by replacing σ with a scalar representation of the instantaneous stress tensor $\boldsymbol{\tau}$, such as, $\sigma = \sqrt{\frac{1}{2}\boldsymbol{\tau} : \boldsymbol{\tau}}$. This method of computing hemolysis is hereafter called "stress-based" method. This method only partially accounts for (**3**) and (**5**) from the aforementioned list of ideal blood-damage model characteristics.

Recently, a tensor-based model for hemolysis prediction was proposed; the model was developed based on an analogy between RBCs and fluid droplets (14,15). In this model, instantaneous deformation of an individual RBC is computed as it flows through the device, and a scalar σ corresponding to an equivalent deformation in a steady simple shear flow is used in eq. 1 (1); this method is called "strain-based," and the details are reported in (14). The strain-based method incorporates several ideal blood-damage model characteristics (**1, 3, 4, and 5**).

Previously, construction and implementation of the strain-based model were demonstrated in (14) for a fictitious two-dimensional blood pump. Here, the performance of the strain-based model is evaluated in a complex 3D time-dependent flow in the GYRO centrifugal blood pump, under development at Baylor College of Medicine, Houston, Texas (16).

In the hemolysis section, the experimental measurements of hemolysis at three typical operating conditions for the GYRO blood pump are reported. Equations governing the blood flow, finite element method-based solution technique, and pathline tracing method are presented. Then, we will briefly recall the strain-based model and present numerical predictions of hemolysis inside the pump for both strain- and stress-based models. Finally a discussion of the results and a summary of this work are presented.

2 HEMOLYSIS EXPERIMENTS

Mock-loop hemolysis experiments were conducted at the Baylor College of Medicine according to the American Society for Testing and Materials (ASTM) standard (13). Three different operating conditions for the horizontal top-contact configuration of the GYRO blood pump were used for these experiments with bovine blood samples. Figure 1 shows the pump in top-contact configuration, in which the impeller and housing are in contact in the top female bearing

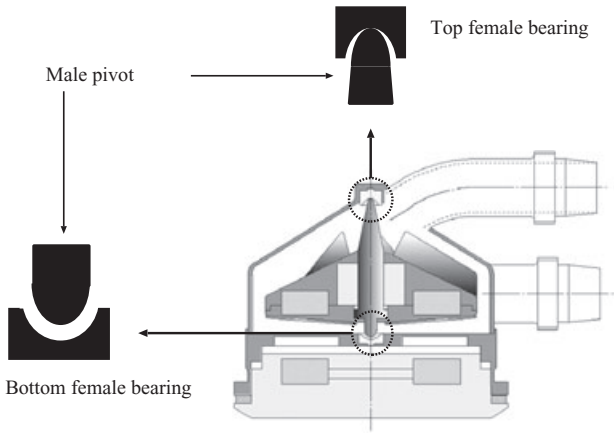

FIG. 1. GYRO pump in top-contact configuration.

and have a finite clearance in the bottom female bearing. In the GYRO pump, the impeller, driven by a magnetic coupling, levitates due to hydraulic lift generated by impeller rotation. The rotation speed at which the impeller levitates is a function of flow conditions and magnetic coupling. The experiments were carried out for 6 h and repeated five times, and the blood was drawn from the sampling port every 60 min. The hemolysis was measured using a TMB (tetra-methyl benzidine) calorimetric assay (Sigma Diagnostic Kit no. 527, St. Louis, MO, U.S.A.). The hemolysis was reported in NIH; based on the ASTM-standard definition, NIH is equivalent to the hemoglobin released per pass of blood volume through the blood pump, therefore it is related to $\frac{\Delta Hb}{Hb}$ as:

$$\text{NIH (g/100 L blood)} = 100 \times \frac{\Delta Hb}{Hb} \times \left(1 - \frac{Hct}{100}\right) \times \kappa, \tag{2}$$

where *Hct* is the blood hematocrit (45% for a healthy person and 37% for normal bovine blood) and κ is the hemoglobin content of blood (150 g/L for a healthy person). Table 1 lists the operating conditions for the in vitro hemolysis experiments. A complete experimental study of hemolysis in various configurations of GYRO pump—vertical top- and bottom-contact, and horizontal top- and bottom-contact—are performed by Yuri et al. (17,18).

3 EQUATIONS GOVERNING BLOOD FLOW AND SOLUTION PROCEDURE

For the hydraulic analysis of the blood flow in a VAD, the basic variables are velocity **u** and pressure p. In a bounded domain Ω with boundary Γ, **u** and p are governed by the momentum and mass conservation equations; for an incompressible fluid,

$$\rho\left(\frac{\partial \mathbf{u}}{\partial t} + \mathbf{u}\cdot\nabla\mathbf{u} - \mathbf{f}\right) - \nabla\cdot\mathbf{T} = \mathbf{0}, \tag{3}$$

$$\nabla\cdot\mathbf{u} = 0, \tag{4}$$

where ρ is blood density (1058 kg/m^3), **u** is velocity, **T** is stress, and **f** denotes body forces per unit mass

TABLE 1. *Operating conditions under consideration for numerical and experimental hemolysis studies*

Operating condition	Orientation	rpm	Flow rate (L/min)	Pressure head (mm Hg)
A	Horizontal, top-contact	1600	3.8	56.5
B	Horizontal, top-contact	2000	5.0	100.0
C	Horizontal, top-contact	2350	6.8	108.0

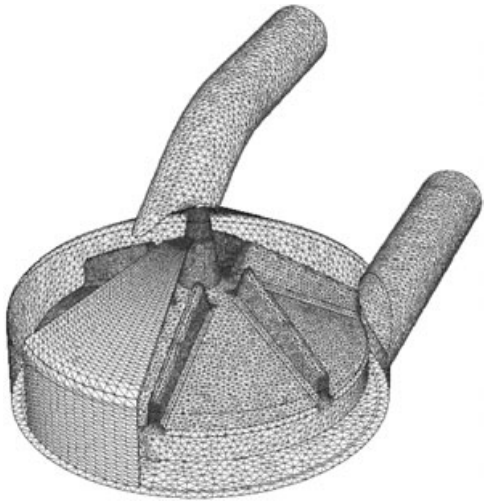

FIG. 2. Finite element mesh showing a portion of the shear slip mesh along with the surface mesh for the GYRO centrifugal blood pump.

(e.g., gravity). Blood is a shear-thinning viscoelastic fluid, however, as a first approximation, it is considered to be a Newtonian fluid, and consequently:

$$\mathbf{T} = -p\mathbf{I} + \boldsymbol{\tau},\ \boldsymbol{\tau} = \mu\,(\nabla\mathbf{u} + \nabla\mathbf{u}^T), \tag{5}$$

where μ is the dynamic viscosity of blood (~3.5 P at high shear rate) and $\boldsymbol{\tau}$ is the viscous stress. In this case, Eqs. 3 and 4 reduce to the incompressible Navier–Stokes equations. Body force is neglected in the analysis presented here.

The well-established deformable-spatial-domain/stabilized space-time (DSD/SST) finite element approach is applied to solve Eqs. 3 and 4 (19,20). The moving impeller of the centrifugal blood pump is treated with the shear-slip mesh update method (SSMUM) (21). Details of the hydraulic performance analysis of the GYRO centrifugal blood pump using the DSD/SST and SSMUM method are reported in (2). A hybrid structured/unstructured finite element mesh, created for the DSD/SST–SSMUM method, is shown in Fig. 2; it consists of 1 017 731 tetrahedral elements and 350 162 space-time nodes. The flow conditions in the pump are prescribed by specifying the impeller rotation speed and velocity profile at the inflow. The impeller is constrained to complete 1 revolution in 100 steps, and the CFD time step is set accordingly. For the operating conditions A, B, and C shown in Table 1, the CFD time steps used are 3.75×10^{-4}, 3.00×10^{-4}, and 2.55×10^{-4} s, respectively. The velocity and pressure data are recorded every five time steps (18° rotation). This implies that the CFD data for different operating conditions are available at intervals of 1.875×10^{-3}, 1.500×10^{-3}, and 1.3043×10^{-3} s, respectively.

The flow and rotation of the impeller are ramped up from zero to the desired value over the initial 40 steps, and data are recorded after the flow is fully developed. Forces on the impeller are used to detect fully developed flow conditions; these forces stabilize after 7–8 revolutions depending on impeller speed and flow rate. The results reported hereafter are computed during the 11th revolution of the impeller. At each time step, four Newton–Raphson iterations are used to solve the nonlinear discretized system, and a generalized minimal residual GMRES (22) solver is used to solve the linear system at each iteration. The computation of 100 time steps required 6 h on 32 processors of a 1.7 GHz Pentium 4 PC cluster.

A forward Euler technique is used to trace pathlines through the pump, and the hemolysis is computed with both stress- and strain-based models in the Lagrangian frame moving along the pathlines. In the case of 3D pump, the storage requirements of a refined CFD data (every time step) are nontrivial, and thus data are stored only for every 18° rotation of the six-vaned impeller. Subsequently, the data required for tracer time steps, which are smaller than CFD time steps by two orders of magnitude, are generated using a linear temporal interpolation between two consecutive CFD time steps. The tracer time steps for the three operating conditions (A, B, and C) shown in Table 1 are 1.125×10^{-5}, 0.900×10^{-5} and 0.786×10^{-5} s, respectively. Details of the tracing procedure employing the forward Euler scheme are presented in (14). One complete rotation of the impeller is simulated at fully developed conditions, and the pathlines are traced through the pump by cycling over this data as shown in Fig. 3. In the figure, solid lines represent the discrete CFD data spaced at every 18° rotation of the impeller. The smaller intervals between the two solid lines represent the tracer time steps; a linear interpolation is employed to obtain data at the tracer locations. After one complete revolution, the CFD data are recycled. This procedure assumes that periodic fully developed flow features in the pump with time periods greater than 1 revolution time are insignificant.

The forward Euler tracing in a sparse CFD data leads to a significant number of pathlines abruptly terminating at the domain walls; the problem persists with reduced tracer time steps. A more accurate but costly scheme of computing pathlines employing fourth order Runge–Kutta method gives the same results, although it allows greater tracer time step size than the forward Euler method. Tracer particles hitting the wall and leaving the fluid domain are only a numerical artifact, and in some commercial postprocessing packages, this problem is dealt with by either terminating the traces leaving the domain or by imposing an elastic collision on the domain walls. The latter case is shown in Fig. 4a. In the case of tracer particles bouncing elastically off the domain walls, continuity of the pathlines is maintained, but a discontinuity in particle orientation presents difficulties for tracer particle-based computations along pathlines, such as cell deformation tracking.

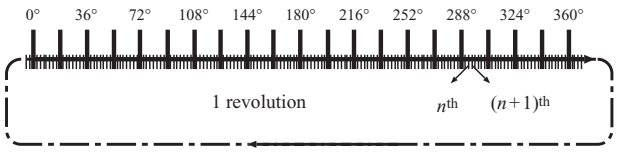

FIG. 3. Discrete CFD scheme for 1 revolution of the impeller and intermediate steps for pathline tracing.

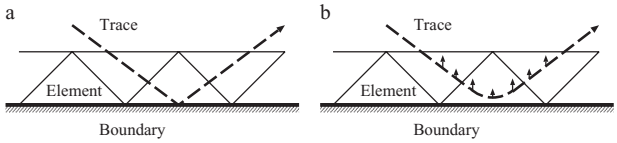

FIG. 4. Particle trace close to the no-slip boundary. Dashed line represents tracer trajectory (a) with elastic bounce on the wall and (b) with wall-repelling force.

A remedy to this problem is devised by introducing a wall-repelling force on the tracer particles. The force is inversely proportional to the distance of the tracer point from the nearest wall, which is computed along with velocity and pressure using an interpolated distance function. The particle trajectory is shown in Fig. 4b; the method ensures a continuity of pathline and particle orientation. Computation of the distance function is further described in the next subsection.

3.1 Wall distance computation

The computation of an exact distance of a tracer point from the closest wall is difficult in the case of unstructured meshes due to the following reasons:

1. The problem is of the order M, for each tracer point at each tracer step, where M is the number of nodes on the boundary.
2. The problem is difficult to parallelize as it requires very high communication, which becomes time-consuming especially for large problems.

The problem is simplified by constructing a partial differential equation (PDE) for an interpolated distance function D, and solving it along with the basic variables of velocity and pressure. The Eikonal equation $\|\nabla D\|^2 = 1$ is the basis for the PDE. Fares et al. (23) proposed a PDE for the interpolated G, which is the inverse of the wall distance $G = 1/D$. Adding a

diffusion and generation term, they proposed the inverse wall distance equation as:

$$\nabla\cdot(G\nabla G) + (\alpha - 1)G\nabla^2 G - \gamma G^4 = 0, \qquad (6)$$

where α and γ are constants.

Here, a term $\alpha G\nabla^2 G$ is added to tune the distance function near the edges and corners, and $\alpha > 0$ as the added term is a diffusion-like term, which must be positive (G is also positive). To compensate for the additional elliptic term, the source term G^4 is multiplied by a factor $\gamma = 1 + 2\alpha$.

At the physical walls of the flow domain (no-slip boundaries) $G_{wall} = g$, and for far-field, inflow, and outflow boundaries, it is assumed that $\mathbf{n}\cdot\nabla G = 0$ ($\mathbf{n}$ is the unit vector normal to the boundary).

3.2 Galerkin formulation for wall distance equation

The Galerkin form of Eq. 6 is given as: Find $G^h \in S_G^h$ such that $\forall W^h \in V_G^h$:

$$\int_\Omega W^h\left[\nabla\cdot(G^h\nabla G^h) + (\alpha - 1)G^h\nabla^2 G^h - \gamma(G^h)^4\right]d\Omega = 0. \qquad (7)$$

The finite element interpolation and weighting function spaces are defined as:

$$S_G^h = [G^h | G^h \in H^{1h}(\Omega), G^h \doteq g^h \text{ on } \Gamma_g], \qquad (8)$$

$$V_G^h = [G^h | G^h \in H^{1h}(\Omega), G^h \doteq 0 \text{ on } \Gamma_g]. \qquad (9)$$

Hereafter, G^h and W^h are referred to as G and W, respectively. In Eq. 7, the first two terms are integrated by parts, and the integrals on boundary Γ_h are dropped as $\mathrm{n}\cdot\nabla G = 0$ on all non-Dirichlet boundaries. The weak form then appears as: Find $G \in S_G^h$ such that $\forall W \in V_G^h$:

$$(1-\alpha)\int_\Omega \nabla(WG)\nabla G d\Omega - \int_\Omega \nabla W\cdot(G\nabla G)d\Omega - \gamma\int_\Omega WG^4 d\Omega = 0 \qquad (10)$$

A 3D implementation of Eq. 10 is employed to compute the wall distance along with the basic variables (velocity and pressure) in the GYRO centrifugal blood pump. A high diffusive parameter ($\alpha = 0.5$) is used to activate the interpolated function only in the first layer of elements along any solid surface. Moreover, the highly diffusive nature of the wall distance function retains the convergence characteristics for the enhanced equation system, thereby reducing the cost of computing an extra unknown.

4 STRAIN- AND STRESS-BASED HEMOLYSIS MODELS

4.1 Strain-based model

The mammalian RBCs are biconcave disks with a viscoelastic membrane that encapsulates Newtonian liquid (hemoglobin), and the cells are suspended in a Newtonian medium (plasma). When blood is at rest, the RBCs form coin stack-shaped structures (rouleaux); these structures break and blood cells are individually suspended when blood is set into motion. Owing to the biconcave shape, an RBC has 40% excess surface area compared to a sphere of the same volume. The excess surface area allows the RBC to undergo both volume and surface area-preserving deformations. It is observed that RBCs assume an ellipsoidal shape and remain oriented along the flow direction in a simple shear flow. This behavior of RBCs is very similar to that of fluid droplets neutrally suspended in another immiscible fluid. Above 10/s shear rate, the RBC loses its biconcave shape, and the RBC membrane begins to stretch, develops pores, and starts releasing its hemoglobin into the plasma, resulting in hemolysis. Barring catastrophic hemolysis, which occurs at shear rates above 42 000/s (24), the RBCs gradually return to their original shape as the shear rate of flow is reduced. The RBCs are also known to show a tank-treading phenomenon under the influence of shear flow, where the viscoelastic membrane of the cell revolves around the enclosed fluid, while the cell remains aligned with the flow.

Based on the analogy between RBCs and neutrally suspended fluid droplets, a blood-damage model is constructed. The shape of the droplets, as well as RBCs, can be represented by a morphology tensor $\mathbf{S}$. Maffetone and Minale (25) proposed a droplet deformation equation, and it is modified here to account for the tank-treading motion shown by the RBCs. Thus, at any instant:

$$\mathbf{S}^{\circ} = -f_1[\mathbf{S} - \varrho(\mathbf{S})\mathbf{I}] + f_2(\tilde{\mathbf{E}}\cdot\mathbf{S} + \mathbf{S}\cdot\tilde{\mathbf{E}}) + f_3(\tilde{\mathbf{W}}\cdot\mathbf{S} - \mathbf{S}\cdot\tilde{\mathbf{W}}), \qquad (11)$$

where:

$$\mathbf{S}^{\circ} = \frac{d\mathbf{S}}{dt} - (\boldsymbol{\Omega}\cdot\mathbf{S} - \mathbf{S}\cdot\boldsymbol{\Omega}), \quad \varrho(\mathbf{S}) = \frac{3III}{II}, \qquad (12)$$

$\tilde{\mathbf{E}}$ and $\tilde{\mathbf{W}}$ are the rate of strain and relative vorticity tensor, respectively, and II and III are second and third invariants of $\mathbf{S}$, respectively:

$$II = \frac{1}{2}\left[\mathrm{tr}(\mathbf{S})^2 - \mathrm{tr}(\mathbf{S}^2)\right], \quad III = \det(\mathbf{S}). \qquad (13)$$

f_1, f_2 and f_3, are constant parameters set according to the physical properties of blood.

To account for the instantaneous rotation of the tank-treading cell, the rotating reference frame defined by the unit eigenvectors $\tilde{\mathbf{e}}_i$ of $\mathbf{S}$ is considered; the rotation tensor $\boldsymbol{\Omega}$ is hence computed as:

$$\mathbf{\Omega} = \tilde{\mathbf{e}}_i \frac{d\tilde{\mathbf{e}}_i}{dt} = \tilde{\mathbf{e}}_i \left(\frac{\partial \tilde{\mathbf{e}}_i}{\partial t} + \mathbf{u} \cdot \nabla \tilde{\mathbf{e}}_i \right). \quad (14)$$

Finally, $\tilde{\mathbf{W}}$ is the relative vorticity $\mathbf{W} - \mathbf{\Omega}$. The first term on the right-hand side of Eq. 11 recovers the shape of the droplet in the absence of a shear flow; this generalized recovery term is made RBC-specific by setting f_1. The second term represents the nonaffine deformation of the droplet. The third term captures the tank-treading motion, which reduces the relative vorticity seen by the droplet. The ellipsoidal shape and orientation are identified by the eigenvalues of **S**. To capture the instantaneous RBC deformation specifically, $f_1 = 5.0$/s. In a steady shear flow of intensity $\dot{g}$, the droplet remains at fixed orientation to the flow ($\mathbf{\Omega} = \mathbf{0}$), and the steady-state droplet deformation equation becomes:

$$f_1[\mathbf{S} - \varrho(\mathbf{S})\mathbf{I}] = f_2(\nabla \mathbf{u} \cdot \mathbf{S} + \mathbf{S} \cdot \nabla \mathbf{u}^T) \quad (15)$$

The L, B, and W, which denote the three semiaxial lengths of the droplet, are easily computed from **S** in Eq. 15. An RBC, which has 40% excess surface area as compared to a droplet of same volume, undergoes 6% areal strain before hemolyzing (26). Therefore, an RBC should stretch to 1.40×1.06 times its original surface area at catastrophic hemolysis. Matching the droplet area with hemolyzing RBC area gives:

$$f_2 = f_3 = 1.25 \times 10^{-3}. \quad (16)$$

The three parameters f_1, f_2, and f_3 together incorporate relaxation time of RBC membrane (~200 ms) (27), tank-treading, and critical areal strain limit into the hemolysis model.

The instantaneous shape of the droplet, obtained from Eq. 11 in a general flow, is used to compute instantaneous shape distortion $\ell = (L-B)/(L+B)$, where L and B are the largest and smallest axis lengths of the ellipsoidal droplet, respectively. An effective steady shear flow intensity $\dot{g}_{\text{eff}}$ corresponding to the distortion ℓ, and steady shear stress σ_{eff} are computed as:

$$\dot{g}_{\text{eff}} = \sqrt{\frac{f_1^2 \ell^2}{(1-\ell^2) f_2^2}}, \quad \sigma_{\text{eff}} = \mu \dot{g}_{\text{eff}}. \quad (17)$$

Because in a steady shear flow, there is a one-to-one correspondence of shear stress and distortion, a strain-based hemolysis model is constructed by requiring that the strain- and stress-based models yield the same results in steady shearing; using rate of hemolysis (time derivative of Eq. 1) along with Eq. 17 yields a strain-based relationship:

$$\frac{d}{dt}\left(\frac{\nabla Hb}{Hb}\right) = 2.8417 \times 10^{-7} \left(\mu_{\text{blood}} \sqrt{\frac{f_1^2 \ell^2}{(1-\ell^2 f_2^2)}} \right)^{2.416} \Delta t^{-0.215} \quad (18)$$

4.2 Stress-based model

In the case of the stress-based models, an instantaneous response of the RBCs to shear is assumed. Thus, a scalar σ is obtained from the instantaneous **T**, for example, $\sigma = \sqrt{\frac{1}{2}\boldsymbol{\tau} : \boldsymbol{\tau}}$, and used directly in Eq. 1

Figure 5 schematically compares the stress- and strain-based hemolysis models in the blood pump. The steady simple shear hemolysis experiment results can be written in two different forms. The traditional stress-based model, which utilizes the instantaneous measure of the stress, is based on the hemolysis-versus-shear-stress form, and the tensor-based model (strain-based) utilizes the instantaneous strain of the RBCs and adopts the hemolysis-versus-strain approach.

4.3 Hemolysis computations along pathlines

The flow is simulated numerically, and then the pathlines are traced through the pump using the forward Euler scheme combined with a wall-repelling force. Thus, along a pathline at the $(n+1)^{\text{th}}$ tracer time step (see Fig. 3), the new tracer position $\mathbf{x}_{n+1}$ is computed as:

$$\mathbf{x}_{n+1} = \mathbf{x}_n + \mathbf{u}\Delta t + \underbrace{X \frac{1-G}{G} |\mathbf{u}\Delta t| \frac{\nabla G}{\nabla G}}_{\text{A1}}, \quad (19)$$

where $\mathbf{x}_n$ is the previous tracer position, **u** is the local velocity of the tracer particle, Δt is the pathline time step size (1.125×10^{-5} s), and A1 is the wall effect proportional to the step size ($\mathbf{x}_{n+1} - \mathbf{x}_n$) acting normal to the wall. For the wall distance computation, $G = 0$ at all physical boundaries, and G is normalized with its maximum value in the domain when computing the increment A1. When A1 = 0, the update reduces to forward Euler method. Parameter χ is selected to

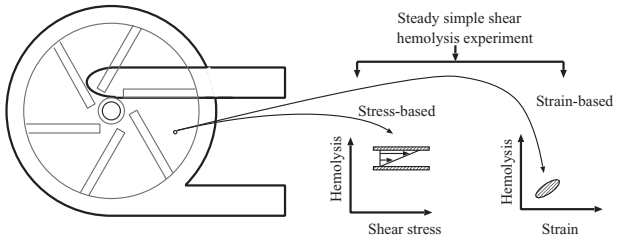

FIG. 5. Stress- and strain-based hemolysis predictions for the centrifugal blood pump.

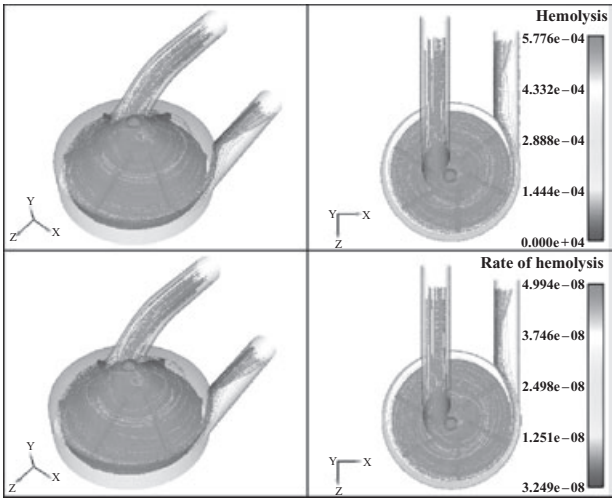

FIG. 6. A set of pathlines through the pump. Top two images show the accumulated hemolysis, while bottom two images show the rate of hemolysis.

ensure that all pathlines introduced at the pump inflow appear at the outflow; typically, $\chi = 1.0$.

The pathline tracing and numerical integration of hemolysis are done with a particle tracing code developed in-house. Figure 6 shows a set of representative pathlines through the pump; the top row depicts the hemolysis accumulated, while the rate of hemolysis is shown in the bottom row. Figure 7 shows two characteristic pathlines; while Figure 7a shows a particle reaching the outlet after 1 revolution through the pump, Figure 7b shows a particle remaining in the pump for a considerably longer time.

To compute statistically meaningful averages with the pathlines, 271 tracer particles are released at the inlet of the pump for each of the three operating conditions. Figure 8a shows the initial positions of the tracer particles at the inlet. The hemolysis accumulated along each pathline is recorded and a simple

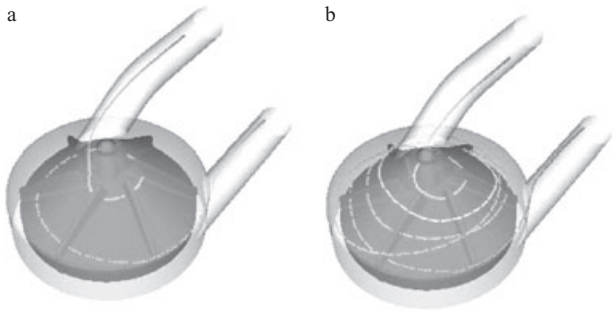

FIG. 7. Two characteristic pathlines through the GYRO pump. Pathline in (a) reaches outlet in 1 revolution, while pathline in (b) remains in pump for 5 revolutions.

average of 271 pathlines at the outlet can be computed to obtain bulk flow hemolysis inside the pump. However, from the initial positions of the tracer particles, it is clear that hemolysis along the wall of the inlet is overrepresented when compared with the flow at the center. Moreover, each pathline represents a volume fraction of the bulk flow, and thus a flow rate weighted average of the 271 pathlines is computed. For a continuous hemolysis field $h(r)$, the volume averaging can be computed as:

$$h_{\text{avg}} = \frac{\int_0^R 2\pi r\, u(r)\, h(r)\, dr}{\int_0^R 2\pi r\, u(r)\, dr}, \qquad (20)$$

where R is the radius of the inlet and $u(r)$ is the velocity along inflow (see Fig. 8a).

The GYRO blood pump has a six-vaned impeller, and under fully developed conditions, the flows past all impeller vanes remain identical. However, the relative position of the impeller and inlet cannula at the time of the release of the tracer particle can significantly affect the pathlines originating from the same point. Thus, for the operating condition A, the 271 pathlines are released at different impeller starting

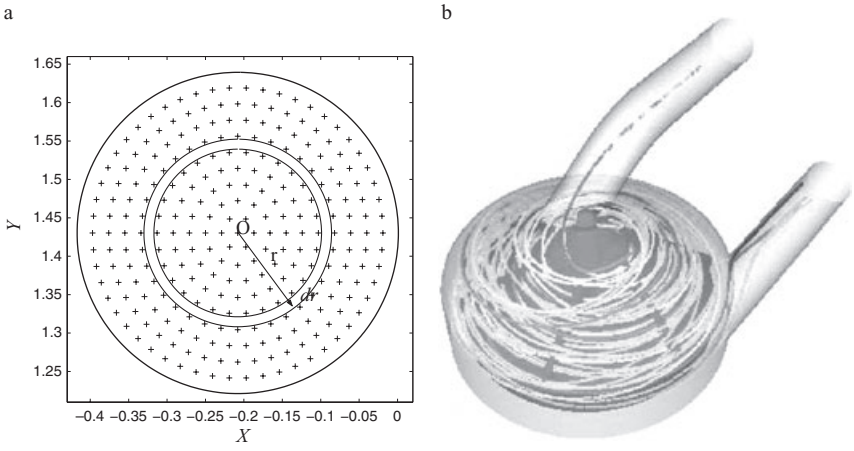

FIG. 8. (a) Initial distribution of tracer particle at the inlet of the pump. (b) Tracer paths originating from O but released at different impeller positions.

TABLE 2. *Comparison of numerical hemolysis prediction using stress- and strain-based methods with experimental hemolysis measurements at three operating conditions of the GYRO pump*

Operating condition	Computational hemolysis (NIH)		Experimental hemolysis (NIH)	
	Stress-based	Strain-based	Mean	SD
0°	0.0378	0.0073	0.0072	na
18°	0.0382	0.0078		
A 36°	0.0385	0.0081		
54°	0.0373	0.0074		
72°	0.0394	0.0075		
Average	0.0382	0.0076		
B	0.0518	0.0084	0.0070	±0.0016
C	0.0945	0.0139	0.0210	na

The experimental hemolysis data were provided by Dr. Koichi Yuri at the Center for Artificial Organ Development, Baylor College of Medicine, Houston [28].

Flow rate-weighted SD values of strain-based hemolysis prediction for operating conditions A, B, and C are 0.00076, 0.00088, and 0.0036, respectively.

na, not available.

positions; this is achieved by releasing the particles at 0°, 18°, 36°, etc., as shown in Fig. 3, and then cycling over the CFD data. Figure 8b shows the pathlines originating from point O shown in Fig. 8a; the pathlines remain concurrent in the inflow cannula but segregate in the housing due to the difference in relative position of the impeller. The periodic release of tracer particle is expected to capture the temporal variations in the pathlines.

Table 2 shows the average hemolysis for the 271 pathlines at the three operating conditions. Specifically, for operating condition A, the averages for different release of tracer particles characterized by the relative impeller position are also presented. A temporal average for the operating condition A is also shown.

Based on the volume of the GYRO centrifugal blood pump (40 mL) and volume flow rates for the cases considered, the average residence time can be estimated for the blood flowing through the pump (estimated residence time is equal to pump volume divided by the flow rate). Table 3 presents the estimated residence time for the three operating conditions, along with the flow rate-weighted average residence time (numerical residence time) for the pathlines traced through the pump. The numerical residence time for the operating condition A is the temporal average of all particles released at regular intervals.

5 DISCUSSION AND SUMMARY

The strain-based blood damage model is constructed based on the physical properties of RBCs, and it is consistent with the steady and unsteady simple shear hemolysis experiments. In this study, the strain- and stress-based models are compared to the experimental measurements of hemolysis in the GYRO centrifugal blood pump at three typical operating conditions. The results from controlled-temperature mock loop hemolysis experiments exclude the blood–air contact and thermal effects, and are thus suitable for validating the current hemolysis models. The numerical hemolysis predictions using the strain-based model are found to be in good agreement with the experimental results. The stress-based model assumes that the RBCs respond to shearing instantaneously and irrespective of the relative orientation of the RBC axes and principal direction of shearing. These assumptions are violated in GYRO blood pump because the intensity of straining and relative orientation of RBC and straining axes change much faster than the RBC relaxation time. Even the strain-based model shows larger deviation from the experimental value at condition C. This is consistent with our past observations that at higher rotation speeds, CFD predictions themselves become less reliable (2), most likely due to shortcomings of the subgrid-scale turbulence model. The blood pumps are complex nonlinear systems, and flow characteristics in these depend highly on the design and operating conditions; an increasing rotation rate can cause dramatic growth of vorticial flow features, which can then trap and damage RBCs.

The hemolysis predictions are made along 271 pathlines traced through the blood pump with a novel technique. Termination of pathlines on the flow domain walls is a common problem when following the tracer particles through discretely represented time-dependent flow data in a complex domain. An elastic bounce on the flow domain walls is a common solution; although it maintains continuity of the pathlines, a discontinuity in orientation of particle appears. A remedy is proposed by imposing a wall-repelling force, which is inversely proportional to the distance from the wall. An interpolated wall distance equation is solved along with the Navier–Stokes equations, and a wall-repelling increment in the direction normal to the flow domain boundary is added to the forward Euler scheme of pathline tracing.

TABLE 3. *Comparison of numerical residence time along the 271 pathlines with estimated residence time obtained from pump volume and respective flow rates*

Operating condition	Numerical residence time (s)	Estimated residence time (s)
A	0.3998	0.666
B	0.2771	0.480
C	0.2411	0.353

The numerical residence time of tracer particles in the flow domain is found to be less than the estimated value. This may be attributed to the presence of a persistent recirculation in the flow domain. Most tracer particles exit the pump by passing near the wall of the outflow tube due to the presence of a previously reported stable eddy (21). The pathlines in the pump pass through the bulk flow volume, and the presence of a stable eddy reduces the volume available for the bulk flow, thereby reducing the residence time.

The prediction of hemolysis with the strain-based model along the pathlines in the Lagrangian framework is shown to be a viable and accurate option for virtual hemolysis prediction.

6 ACKNOWLEDGMENTS

This work was supported by the National Science Foundation under award CTS-ITR-0312764, and computational resources were provided by the National Partnership for Advanced Computational Infrastructure (NPACI), by the Rice Computational Engineering Cluster, funded by NSF through an MRI award EIA-0116289, and by the Rice Terascale Cluster funded by NSF under grant EIA-0216467, Intel, and Hewlett-Packard. The authors acknowledge suggestions and help from Prof. Fazle Hussain and Mr. Tomas Soltys. And finally, the authors are grateful to Dr. Koichi Yuri for the experimental hemolysis data as well as for discussions and suggestions, and Dr. Motomura and Prof. Nosé for access to the experimental facilities at the Center for Artificial Organ Development, Baylor College of Medicine, Houston, TX.

REFERENCES

1. Antaki JF, Ghattas O, Burgreen GW, He B. Computational flow optimization of rotary blood pump components. *Artif Organs* 1995;19:608–15.
2. Behr M, Arora D, Nosé Y, Motomura T. Performance analysis of ventricular assist devices using finite element flow simulation. *International Journal for Numerical Methods in Fluids* 2004;46:1201–10.
3. Hellums JD, Brown CD III. Blood cell damage by mechanical forces. In: Hwang NHC, Normann NA, eds. *Cardiovascular Flow Dynamics and Measurements*. Baltimore, MD: University Park Press, 1977;799–823.
4. Heuser G, Opitz R. A Couette viscometer for short time shearing of blood. *Biorheology* 1980;17:17–24.
5. Hashimoto S. Erythrocyte destruction under periodically fluctuating shear rate: comparative study with constant shear rate. *Artif Organs* 1989;13:458–63.
6. Giersiepen M, Wurzinger LJ, Opitz R, Reul H. Estimation of shear stress-related blood damage in heart valve prostheses—*in vitro* comparison of 25 aortic valves. *Int J Artif Organs* 1990;13:300–6.
7. Yeleswarapu KK, Antaki JF, Kameneva MF, Rajagopal KR. A mathematical model for shear-induced hemolysis. *Artif Organs* 1995;19:576–82.
8. Bludszuweit C. Three-dimensional numerical prediction of stress loading of blood particles in a centrifugal pump. *Artif Organs* 1995;19:590–6.
9. Pinotti M, Rosa ES. Computational prediction of hemolysis in a centrifugal ventricular assist device. *Artif Organs* 1995;19: 267–73.
10. Mitoh A, Yano T, Sekine K, et al. Computational fluid dynamics analysis of an intracardiac axial flow pump. *Artif Organs* 2003;27:34–40.
11. Chan WK, Wong YW, Ding Y, Chua LP, Yu SCM. Numerical investigation of the effect of blade geometry on blood trauma in a centrifugal blood pump. *Artif Organs* 2002;26: 785–93.
12. Schmid-Schönbein H, Wells R. Fluid drop-like transition of erythrocytes under shear. *Science* 1969;165:288–91.
13. American Society for Testing and Materials. Standard practice for assessment of hemolysis in continuous flow blood pumps. Standard F 1841–97, ASTM.
14. Arora D, Behr M, Pasquali M. A tensor-based measure for estimating blood damage. *Artificial Organs* 2004;28:1002–15.
15. Arora D, Behr M, Coronado O, Pasquali M. Estimation of hemolysis in centrifugal blood pumps using morphology tensor approach. In: Bathe KJ, ed. *Proceedings of the Third MIT Conference on Computational Fluid and Solid Dynamics*. Massachussetts: Elsevier, Cambridge, 2005;578–82.
16. Nosé Y, Yoshikawa M, Murabayashi S, Takano T. Development of rotary blood pump technology: Past, present, and future. *Artificial Organs* 2000;24:412–20.
17. Yuri K, Iwahashi H, Motomura T, Hata A, Asai T, Nosé Y, Arora D, Behr M, Pasquali M. Different levels of hemolysis occurred by a centrifugal blood pump in various clinical conditions. *ASAIO Journal (ASAIO 50th Anniversary Conference Abstracts)* 2004;50:121.
18. Yuri K, Iwahashi H, Motomura T, Tanaka A, Nosé Y, Arora D, Behr M, Pasquali M. Different levels of hemolysis induced by a centrifugal blood pump in various clinical conditions. Submitted to *Artificial Organs*, 2004.
19. Tezduyar TE, Behr M, Liou J. A new strategy for finite element computations involving moving boundaries and interfaces – the deforming-spatial-domain/space-time procedure. I. The concept and the preliminary tests. *Comput Methods Appl Mech Eng* 1992;94:339–51.
20. Tezduyar TE, Behr M, Mittal S, Liou J. A new strategy for finite element computations involving moving boundaries and interfaces—the deforming-spatial-domain/space-time procedure. II. Computation of free-surface flows, two-liquid flows, and flows with drifting cylinders. *Comput Methods Appl Mech Eng* 1992;94:353–71.
21. Behr M, Arora D. Shear-slip mesh update method: Implementation and applications. *Computer Methods in Biomechanics and Biomedical Engineering* 2003;6:113–23.
22. Saad Y, Schultz M. GMRES: a generalized minimal residual algorithm for solving nonsymmetric linear systems. *SIAM J Sci Stat Comp* 1986;7:856–69.
23. Fares E, Schröder W. A differential equation for approximate wall distance. *Int J Numer Methods in Fluids* 2002;39:743–62.
24. Leverett LB, Hellums JD, Alfrey CP, Lynch EC. Red blood cell damage by shear stress. *Biophys J* 1972;12:257–73.
25. Maffettone PL, Minale M. Equation of change for ellipsoidal drops in viscous flow. *J Non-Newtonian Fluid Mech* 1998;78: 227–41.
26. Blackshear PL, Blackshear GL. Mechanical hemolysis. In: Skalak R, Chien S, eds. *Handbook of Bioengineering.* New York: McGraw-Hill, 1987;15.1–15.19.
27. Hénon S, Lenormand G, Richert A, Gallet F. A new determination of the shear modulus of the human erythrocyte membrane using optical tweezers. *Biophys J* 1999;76:1145–51.
28. Arora D, Hussain F, Behr M, Pasquali M, Yuri K, Motomura T, Nosé Y. Predictions and measurements of mechanical hemolysis in implantable centrifugal blood pump. *ASAIO Journal (ASAIO 51st Anniversary Conference Abstracts)* 2005;51:1A.